The Beaufort Gyre Extent, Shape, and Location Between 2003 and 2014 From Satellite Observations

Heather C. Regan, Camille Lique, Thomas W. K. Armitage

JGR Oceans

RESEARCH ARTICLE
10.1029/2018JC014379

Special Section:
Forum for Arctic Modeling and Observational Synthesis (FAMOS) 2: Beaufort Gyre phenomenon

The Beaufort Gyre Extent, Shape, and Location Between 2003 and 2014 From Satellite Observations

Heather C. Regan[1], Camille Lique[1], and Thomas W. K. Armitage[2]

[1]Univ. Brest, CNRS, IRD, Ifremer, Laboratoire D'Océanographie Physique et Spatiale, IUEM, Brest 29280, France, [2]Jet Propulsion Laboratory, California Institute of Technology, Pasadena, CA, USA

Abstract The Beaufort Gyre is a significant reservoir of freshwater in the Arctic. It is thought to play a key role in regulating Arctic freshwater discharge to the North Atlantic, and in recent decades its freshwater content has increased in a time of rapid Arctic change. Despite this, its exact dynamical behavior is not fully understood. Here, we make use of an Arctic-wide dataset of dynamic ocean topography, including data under sea ice, to characterize the time-varying extent, shape, and location of the Beaufort Gyre. We show that the gyre expanded toward the northwest between 2003 and 2014, resulting in increased proximity to the Chukchi Plateau and Mendeleev Ridge by 2014. We find that the gyre strength and maximum dynamic ocean topography both respond readily to changes in intensity of the surface forcing, but the gyre area is additionally affected by the location of the Beaufort Sea High. This results in expansion over the Chukchi Plateau and increased asymmetry of the gyre as it becomes constrained by the shallow bathymetry. The gyre strength is correlated with the integrated surface stress on the ocean over the previous 3 months. We discuss the implications of the expansion over shallow bathymetry on gyre dynamical behavior and the potential impacts on the physical properties in the Canada Basin.

Plain Language Summary The Beaufort Gyre, in the Canadian Basin of the Arctic Ocean, contains a large amount of the total freshwater held in the Arctic and is thought to be important in controlling freshwater exported out into the North Atlantic and thus affects the oceanography there. Recently, the freshwater in the gyre has increased, but the gyre itself and the effect of this change are not well understood. We use a satellite dataset to describe, in detail, the size, shape, and position of the gyre, and how it changed over 2003–2014. We found that the gyre circulation increases when winds strengthen, with a delayed response of 3 months. The spatial distribution of the wind also affects the position and shape of the gyre. The gyre expanded toward the northwest until it reached shallow bathymetry, which limited free expansion and caused its shape to become asymmetrical. We discuss the potential effects of this on the gyre's circulation and freshwater storage, as well as impacts on the surrounding ocean.

Key Points:
- Dynamic ocean topography shows the Beaufort Gyre area expanded at a rate of 53,000 km^2/year over 2003-2014, with elevated gyre center from 2007–2012
- Gyre strength is determined by the intensity of the Beaufort Sea High, while its area is also determined by the Beaufort Sea High location
- Shallow bathymetry of Chukchi Plateau restricts westward expansion, resulting in asymmetry and potential changes to gyre dynamics

Correspondence to:
H. C. Regan,
heather.regan@ifremer.fr

Citation:
Regan, H. C., Lique, C., & Armitage, T. W. K. (2019). The Beaufort Gyre extent, shape, and location between 2003 and 2014 from satellite observations, *Journal of Geophysical Research: Oceans*, *124*, 844–862. https://doi.org/10.1029/2018JC014379

Received 26 JUL 2018
Accepted 14 JAN 2019
Accepted article online 16 JAN 2019
Published online 1 FEB 2019

1. Introduction

The Arctic Ocean is an important feature of the global hydrological cycle, through its roles of supplying freshwater to the North Atlantic and storing large quantities of freshwater within its interior (Carmack et al., 2016). Variability of Arctic freshwater export to the North Atlantic has the potential to affect the global thermohaline circulation (Broecker, 1997; Jahn & Holland, 2013) and has been linked to previous salinity anomalies in the subpolar region (e.g., Belkin, 2004; Belkin et al., 1998; Dickson et al., 1988; Karcher et al., 2005). The surface layer of the Arctic contains over 100,000 km^3 of freshwater (Haine et al., 2015) due to a combination of input from terrestrial river runoff, a net precipitation over evaporation, inflow of fresh Pacific Water through Bering Strait, and advection and seasonal melting of sea ice. The freshwater budget of the Arctic Basin is a three-way balance between the various freshwater sources and sinks to/from the Arctic Basin and the variations of the freshwater storage (Lique et al., 2009), the latter occurring mainly in the Beaufort Gyre (BG) of the Canada Basin (Aagaard & Carmack, 1989; Haine et al., 2015). The freshwater content is known to vary on seasonal to decadal timescales in response to changes to wind stress (Proshutinsky et al., 2002). Previous studies have suggested that an increase of the BG freshwater content could be associated with a spin-up of the gyre, resulting from persistent anticyclonic atmospheric forcing (Armitage et al., 2017; Giles et al., 2012; McPhee, 2013). In contrast, the BG freshwater content could vary independently from the area of the gyre (Proshutinsky et al., 2009). The overall amount of freshwater stored

in the BG increased during the 1990s to 2000s (e.g., Rabe et al., 2011), although the freshwater accumulation has potentially stabilized in more recent years (Krishfield et al., 2014; Zhang et al., 2016). Increased freshwater content could have potential impacts on biological activity via an increase of the depth at which the available nutrients are located in the Canada Basin and therefore a restriction on their availability to phytoplankton (Coupel et al., 2015). Documenting the characteristics of the BG since 2003 is the focus of the present study.

The BG is a large-scale anticyclonic oceanic circulation (Aagaard & Carmack, 1989). It is primarily driven by the persistent Beaufort Sea High (BSH) atmospheric pressure system residing over the region (Serreze & Barrett, 2011), with anticyclonic wind stress forcing fresh surface water convergence in the center of the BG where it downwells via Ekman pumping (e.g., Proshutinsky et al., 2002). The resulting freshwater accumulation depresses the isohalines and is reflected by doming of the sea surface height (SSH) at the center (e.g., Giles et al., 2012). Theoretical and numerical modeling based on idealized process models have suggested that the main dynamical balance of the BG is between Ekman pumping and eddy salt fluxes arising from baroclinic instability that tend to arrest the steepening of the isohalines through lateral salt fluxes (Davis et al., 2014; Manucharyan et al., 2016). Other recent studies have shown that, when the ocean speed approaches that of the ice, the Ekman convergence can be modulated or canceled due to the resulting reduction in the ice-ocean stress (e.g., Dewey et al., 2018; Meneghello, Marshall, Campin, et al., 2018; Meneghello, Marshall, Timmermans, & Scott, 2018; Zhong et al., 2018) in an apparent negative feedback mechanism (e.g., Meneghello, Marshall, Campin, et al., 2018). The balance between these three processes is established over a decadal timescale, suggesting that the variations of the BG freshwater content carry the imprint of a decade or more of the atmospheric forcing (Johnson et al., 2018). Additional processes such as the generation of topographic Rossby waves could also play a role in the equilibration of the BG (Zhao & Timmermans, 2018).

A modeling study suggested the BSH varies over a 10- to 15-year cycle, oscillating between a strong anticyclonic state and a weaker anticyclonic (or sometimes cyclonic) state (Proshutinsky & Johnson, 1997), and the different phases have been linked with variations of the freshwater storage within the BG (Proshutinsky et al., 2002, 2015). Moreover, the location of the BSH can also vary over time, and its center is not always over the ocean (Moore, 2012), potentially causing a shift in the location of the BG (Armitage et al., 2017).

Movement and/or expansion of the BG within the Canada Basin in response to a change of the intensity or location of the BSH may alter the interaction of the BG with the continental slope and thus its dynamical balance. This effect has been largely ignored so far from the theoretical and numerical modeling studies investigating the dynamics of the BG (Davis et al., 2014; Manucharyan et al., 2016), except for the study by Yang et al. (2016) that suggests that the presence of the North Alaskan and Chukchi plateaus could enable the development of a boundary current, similar to the role played by a western boundary for any typical midlatitude gyre. Moreover, it is clear that the presence of shallow bathymetry (around 300 m) in the southwestern side of the BG would lead to the emergence of gyre asymmetry if the gyre were to expand, particularly as the halocline can be 150 m or deeper (e.g., Manucharyan & Spall, 2016; Timmermans et al., 2017). However, the presence of sea ice in the Arctic has prevented us from obtaining a full description of BG behavior based on in situ and satellite observations, as has routinely been done for gyres located in other regions of the globe (e.g., Foukal & Lozier, 2017; Häkkinen & Rhines, 2004). The recent satellite-derived SSH product for the ice-covered region of the Arctic, initiated by Giles et al. (2012) and further developed by Armitage et al. (2016, 2017), enables us to carry out this analysis. SSH is a surface measurement that reflects bulk changes in the water column. As, in the cold Arctic environment, density is almost entirely determined by salinity, SSH variability thus reflects variations in freshwater in the surface layer due to either a salinity change or an increased halocline thickness. In the western Arctic, advection of Pacific Water through the Bering Strait can drive SSH variations, although these are thought to be primarily linked to shelf SSH (Danielson et al., 2014; Peralta-Ferriz & Woodgate, 2017) rather than SSH of the BG. It has been shown that changes in SSH reflect changes in halocline freshwater distribution in the Canada Basin, and thus the SSH field can give useful insights about the 3-D structure of the BG and its variability (Armitage et al., 2016; Giles et al., 2012; Morison et al., 2012). In this study we use the SSH product of Armitage et al. (2016, 2017) to quantify the seasonal and interannual variability and long-term trend of the BG's center (and its location), strength, size, shape, and location and to assess its asymmetry over the period 2003–2014. Constraining these fields

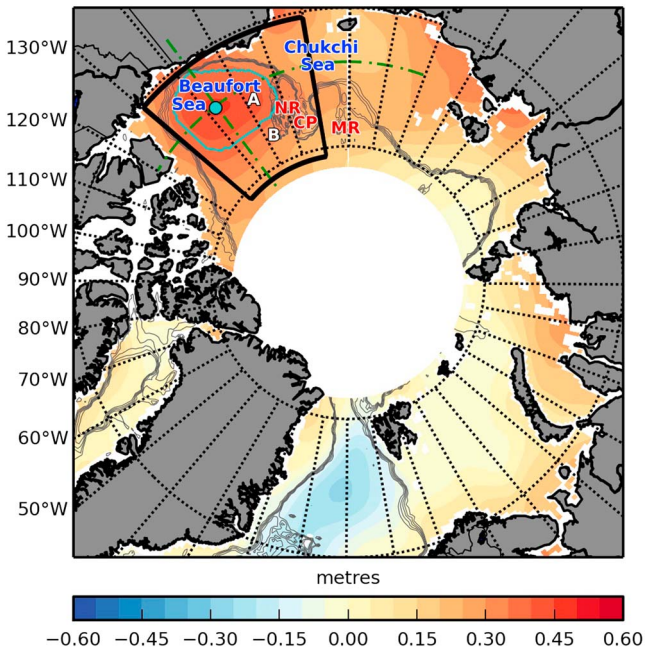

Figure 1. Average 2003 dynamic ocean topography in the Arctic from Armitage et al. (2016), with the 2003 average Beaufort Gyre (BG) extent, computed by the closed contour method (Proshutinsky & Johnson, 1997), and its maximum height shown in cyan. Also shown are the Beaufort and Chukchi seas, the Northwind Ridge (NR), the Chukchi Plateau (CP), and the Mendeleev Ridge (MR). Bathymetry contours at 500, 1,000, 1,500, and 2,000 m are shown in gray. The BG box, a standard region used to describe the BG, is shown in black (Proshutinsky et al., 2009). Example latitude and longitude sections through the center of the gyre, used for Hovmöller plots in section 4.2, are shown in green. Moorings A and B from the Beaufort Gyre Exploration Project (Proshutinsky et al., 2009) are also labeled.

will provide new insight into BG dynamics, in relation to recent environmental changes occurring in the Canada Basin.

Section 2 describes the datasets and metrics used to define the BG and its properties and the computations used to analyze the forcing driving the variations of the gyre. Section 3 provides an in-depth description of the BG and the links between the properties analyzed. In section 4 we investigate the behavior of the gyre described in section 3 in relation to its forcings and physical setting, namely, the strength and position of the surface forcing, and the relative importance of these compared to bathymetric constraints. We discuss the implications of this for observations and the surrounding environment. We conclude in section 5.

2. Methods

2.1. Datasets

The present analysis is based on an altimetry-derived SSH dataset for the ice-covered and ice-free Arctic (Armitage et al., 2016), which spans 2003–2014 with monthly resolution. The reader should refer to Giles et al. (2012) and Armitage et al. (2016, 2017) for a full description of the low-level altimeter processing. Briefly, SSH is estimated from openings in the sea ice pack in ice-covered regions, and this is combined with conventional open ocean altimetry in the ice-free regions to produce monthly SSH composites. Dynamic ocean topography (DOT) is then estimated as the SSH relative to the GOCO03s geoid (Mayer-Gürr et al., 2012). The DOT data are provided as monthly means with 0.25° and 0.75° resolution in the meridional and zonal directions respectively. We use data from the Envisat satellite between 2003 and 2010, providing coverage up to 81.5°N, and this is combined with data from CryoSat-2 between 2011 and 2014, which provides extended coverage up to 88°N. As an example of this dataset, Figure 1 shows the time average DOT across the Arctic for the year 2003.

The BG is driven by atmospheric forcing and constrained by bathymetry, and we examine these in order to understand the variations of the BG derived from the DOT. The bathymetry used is the General Bathymetric Chart of the Oceans bathymetry (Weatherall et al., 2015). We take 10-m wind velocities, $\mathbf{u}_a$, and sea level pressure (SLP) from the twice daily output of ERA-Interim reanalysis (Dee et al., 2011) and average them into daily fields for computation. We also use the National Snow and Ice Data Center sea ice concentration data, α (Comiso, 2017), and ice velocity data, $\mathbf{u}_i$ (Tschudi et al., 2016), and surface geostrophic ocean velocity, $\mathbf{u}_g$, from Armitage et al. (2017).

To make the link between variations of the gyre's DOT and freshwater content, we use freshwater observations from the Beaufort Gyre Exploration Project (BGEP), a combination of summer conductivity-temperature-depth (CTD) and mooring measurements collected from 2003 onwards during summer surveys (Proshutinsky et al., 2009). The gridded dataset (described in Proshutinsky et al., 2009; updated each year) is computed as a height of freshwater in the water column, in meters, by calculating the depth-integrated freshwater content relative to a reference salinity of 34.8, and then interpolated onto a grid with 50 × 50 km grid cells spanning the BG box. It therefore provides a map of summer freshwater content for each year. We make use of the maximum freshwater content (meters) within the gyre and the total freshwater volume (km^3) within the BG box (black box in Figure 1; Proshutinsky et al., 2009) after interpolating the gridded data onto our data grid.

2.2. Gyre Metrics

To define the gyre, we first find the maximum DOT within 140–280°E, 68–81.5°N. This is always the maximum height of the BG (verified by visual inspection). We then find the lowest closed contour of the DOT around this maxima to within 0.1 cm, in line with Proshutinsky and Johnson (1997), which we define as the edge of the BG. This is a slightly different approach to other studies of the region (e.g., Meneghello, Marshall, Timmermans, & Scott, 2018; Proshutinsky et al., 2009), which describe the gyre region by longitudinal

constraints and depths greater than 300 m. Armitage et al. (2017) also define the edge by the largest closed contour but maintain the 300 m restriction. As we are interested in interactions between the BG and bathymetry, we do not impose a depth constraint, and therefore, while Armitage et al. (2017) found a few instances toward the beginning of the data time period where no defined BG occurred, the additional inclusion of DOT contours overlying bathymetry shallower than 300 m here results in a closed contour in all months. For analysis involving the annual average or the monthly climatology of the BG, we average the raw DOT fields first before computing the maximum DOT and area. The center and the DOT contour defining the 2003 average BG are shown in Figure 1.

Throughout most of this study we compute our metrics for the gyre itself (defined by the closed contour), but where more appropriate we use the traditional approach of defining a static box, which we refer to from here on as the "BG box," spanning 70.5–80.5°N, 190–230°E (black box in Figure 1, as in Proshutinsky et al., 2009; note that, as we do not use their 300 m limit to constrain the closed contour, we do not impose this depth limit on the BG box either).

We then use the following metrics to characterize the gyre:

1. *Maximum DOT*—The maximum DOT within the western Arctic (140–280°E, 68–81.5°N, northern limit of the dataset). We define this as the gyre center.
2. *Gyre centroid*—Defined as $(x_c, y_c) = \frac{\sum(x_i,y_i)\mathrm{DOT}_i}{\sum \mathrm{DOT}_i}$, where (x_i, y_i) and DOT_i are the location and DOT at each point i within the BG, as used by Armitage et al. (2017). The difference between the location of the maximum DOT and the gyre centroid provides an indication of gyre asymmetry.
3. *Minimum DOT*—The average DOT along the gyre edge (the largest closed contour around the maximum DOT).
4. *Area*—The area enclosed by the largest closed contour surrounding the maximum DOT.
5. *Strength*—We compute the strength, S, following Proshutinsky and Johnson (1997), as

$$S = \frac{\mathrm{DOT}_{\max} - \mathrm{DOT}_{\min}}{\bar{R}}, \tag{1}$$

   where $\bar{R}$ is the mean radius of the gyre, calculated as the distance between the normal to the maximum and minimum DOT contours. Computing S with $\bar{R}$, $R_{\max}$ and $R_{\min}$ results in highly correlated time series, and thus, S is not significantly affected by the choice of R.
6. *Spatial gradient of DOT*—The magnitude of the lateral slope at each grid cell, defined as lateral slope $= \sqrt{(\frac{\mathrm{dDOT}}{\mathrm{d}x})^2 + (\frac{\mathrm{dDOT}}{\mathrm{d}y})^2}$ and displayed as a map.

2.3. Atmospheric Forcing

We consider the estimate of the surface stress, τ_{tot}, taking into account the presence of sea ice and the ocean geostrophic circulation, following the method of Meneghello et al. (2017) and Meneghello, Marshall, Timmermans, and Scott (2018), so that

$$\tau_{\mathrm{tot}} = \alpha\tau_{\mathrm{ice}} + (1-\alpha)\tau_{\mathrm{atm}}, \tag{2}$$

where α, the sea ice concentration, determines the contribution from the wind stress, τ_{atm}, and ice-ocean stress, τ_{ice}. Here, the stress terms are computed as

$$\tau_{\mathrm{atm}} = \rho_a C_{Da} |\mathbf{u}_a| \mathbf{u}_a, \tag{3}$$

where $\rho_a = 1.25\ \mathrm{kg/m^3}$ is the air density and $C_{Da} = 0.00125$ is the air ocean drag coefficient, using the same constants as in Ma et al. (2017), and

$$\tau_{\mathrm{ice}} = \rho C_{Di} |\mathbf{u}_{\mathrm{rel}}| \mathbf{u}_{\mathrm{rel}}, \tag{4}$$

where $\rho = 1{,}027.5\ \mathrm{kg/m^3}$ is the water density and $C_{Di} = 0.0055$ is the air ocean drag coefficient as used in Meneghello, Marshall, Timmermans, and Scott (2018), and $\mathbf{u}_{\mathrm{rel}} = (\mathbf{u}_i - \mathbf{u}_g)e^{i\beta}$ is the ice-ocean relative velocity as in Dewey et al. (2018) and Meneghello, Marshall, Campin, et al. (2018), with a turning angle, $\beta = 23°$, accounting for the Ekman layer (Dewey et al., 2018; McPhee, 1980).

We use both the full computation of τ_{tot} and also the case where we ignore sea ice and consider the effect of just the wind by setting $\alpha = 0$. In each case we compute vertical Ekman velocity, w_{Ek}, following Meneghello, Marshall, Timmermans, and Scott (2018), so that

$$w_{\mathrm{Ek}} = \frac{\nabla \times \tau_{\mathrm{tot}}}{\rho f}, \tag{5}$$

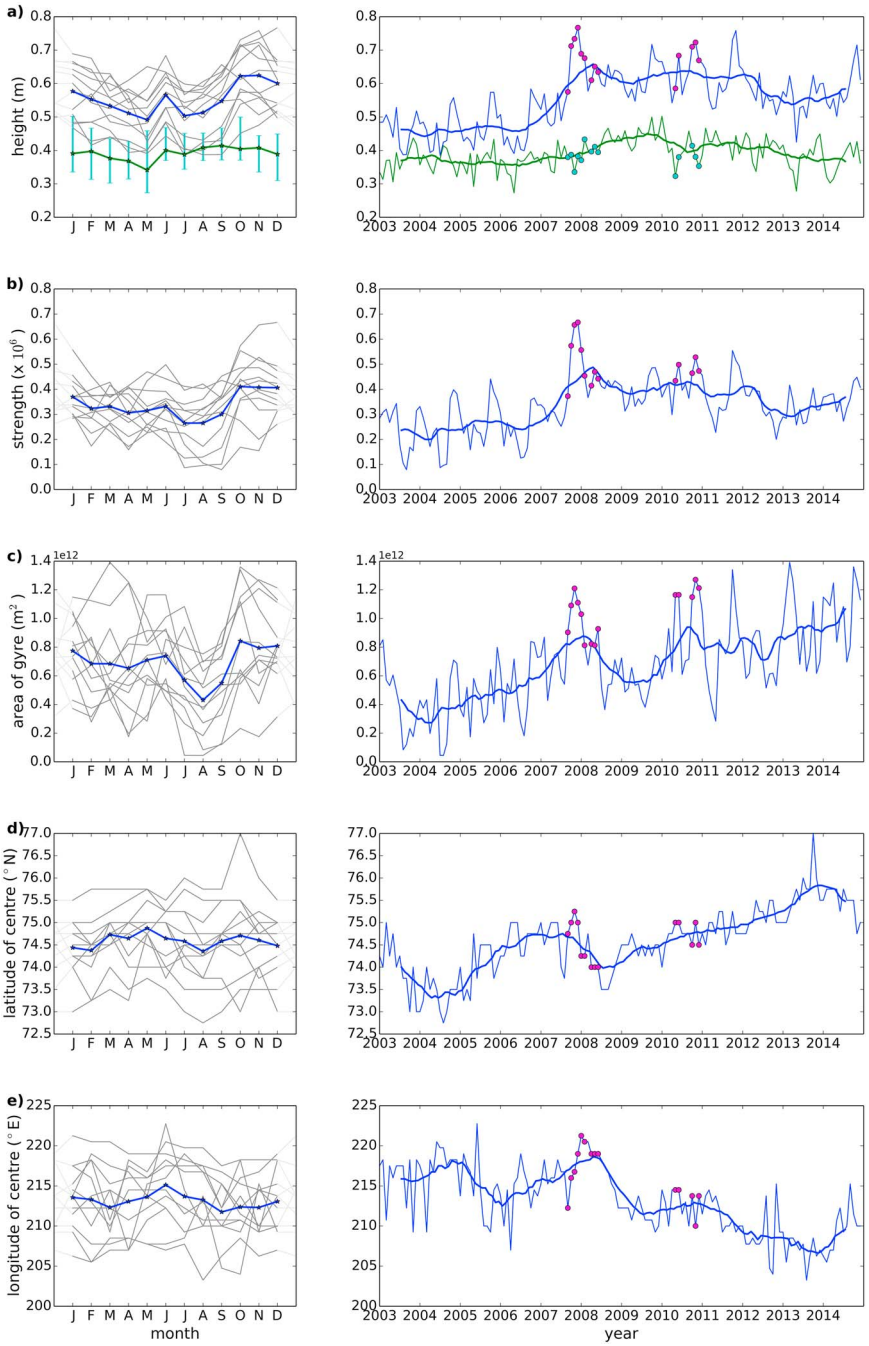

Figure 2. Seasonal cycle (left column) overlaid on individual years (gray), and time series (right column) of (a) maximum gyre dynamic ocean topography (blue) and minimum gyre dynamic ocean topography (green; range of individual years shown in cyan), (b) strength of the gyre, $\times 10^6$ (equation (1)), (c) gyre area, (d) latitude of gyre center, and (e) longitude of gyre center. Thick line (right) represents the 12-month running mean. Months where the northern bound of the gyre is limited by the northern limit of 81.5°N of the data before 2011 are highlighted by magenta/cyan dots.

where f is the Coriolis parameter. The comparison of Ekman pumping computed from the two estimates of the surface stress (including, or not, the presence of sea ice) provides insight into the importance of the presence of sea ice and the role of ocean currents for BG dynamics (see section 4). We compute area-averaged surface forcing over the BG box.

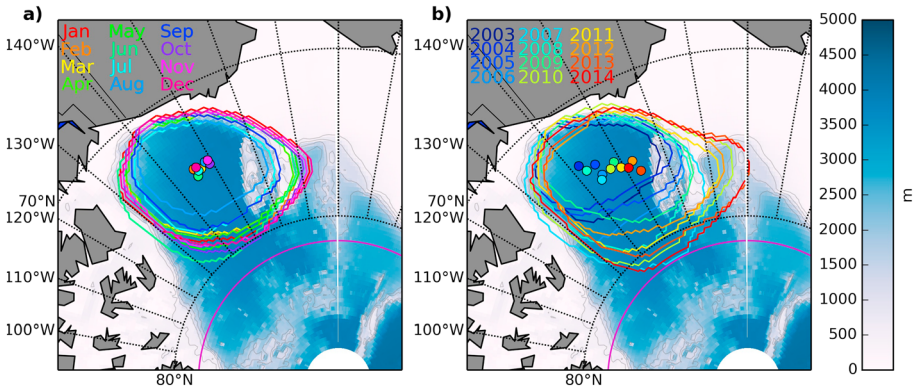

Figure 3. (a) The monthly climatological extent and (b) annual average extent of the Beaufort Gyre from 2003–2014, as defined by the largest closed contour of dynamic ocean topography. The location of the maximum dynamic ocean topography for each contour is also shown. Overlaid on General Bathymetric Chart of the Oceans bathymetry of the Arctic (with contours at 500, 1,000, 1,500, and 2,000 m drawn in gray) with the 2003–2010 northern limit of the dataset, at 81.5°, shown in magenta.

3. Seasonal and Interannual Variability of the Gyre

The aim of this section is to characterize different dynamical aspects of the BG based purely on the DOT fields and their seasonal and interannual variations, as well as their long-term trends. We focus on the maximum DOT, average strength, size, and position of the gyre (Figure 2), the location of the gyre (Figure 3), and its intensity, computed as the lateral gradient of DOT (Figures 4 and 5). Figure 6 shows the interannual variations of the center of the gyre, its weighted center, and seasonal and interannual time series of the distance between the two, providing indications of gyre asymmetry.

3.1. Seasonal Variability

We first examine the seasonal variations of the gyre metrics, based on average values for each month over 2003–2014 (Figures 2 and 3a). From Empirical Orthogonal Function analysis, Armitage et al. (2016) found that the seasonal cycle of the Arctic SSH accounts for 40% of the total variance. We note that a long-term trend (section 3.2) may drive a part of the variability observed in the monthly climatology, and therefore we only discuss the seasonal cycle when it is significant and consistent across several years (Figure 2, gray lines). Figure 3a shows a map of the mean seasonal cycle of the gyre area over 2003–2014. The gyre is smallest in August/September, with a northward and westward expansion to its largest westward extent in November–December where it resides over the Chukchi Plateau. It remains large until late spring before shrinking in summer, with the August extent ($430.5 \pm 236.9 \times 10^3$ km^2) almost half of its maximum seasonal extent in October ($843.3 \pm 344.8 \times 10^3$ km^2). Note that these values may be slightly underestimated due to the gyre extending beyond the northern limit of the dataset in the winters of 2007–2008 and 2010–2011 and additionally in May–June of 2010 (magenta dots on Figure 2). There is little seasonality in the position of the center of the gyre (Figures 2d and 2e), which tends to vary more on an interannual to decadal timescale.

Like the gyre area, the maximum DOT and BG strength exhibit a large seasonal cycle (Figure 2), with a peak in October–November and reduction in the summer in all but 2 years. The gyre strength is roughly constant from February to May, due to a decrease in both maximum and minimum DOT, resulting in similarity between the seasonal cycles of BG strength and area (though both metrics display high variability during spring, with particularly large deviation from the mean seasonal cycle in March). There is a distinctive rise of maximum and minimum DOT from May to June in all but 2 years, with an increase of 0.07 m ± 0.03 and 0.06 m ± 0.05, respectively, between the 2 months. After June, the minimum DOT remains high, peaking in August–September when the area and maximum DOT are low, resulting in a reduction of BG strength (Figure 2b, left panel) from July to September. Figure 4 shows that, throughout the year, the southern portion of the BG, and in particular the southwest (which is bounded by shallow bathymetry), has increased flow compared to the north, but this is particularly amplified from October to December as the BG expands toward the coast.

The two-peaked significant seasonal cycle visible in the maximum DOT (Figure 2a, left panel) aligns well with the seasonal cycle of both mean Arctic DOT and BG steric height previously described by Armitage et al.

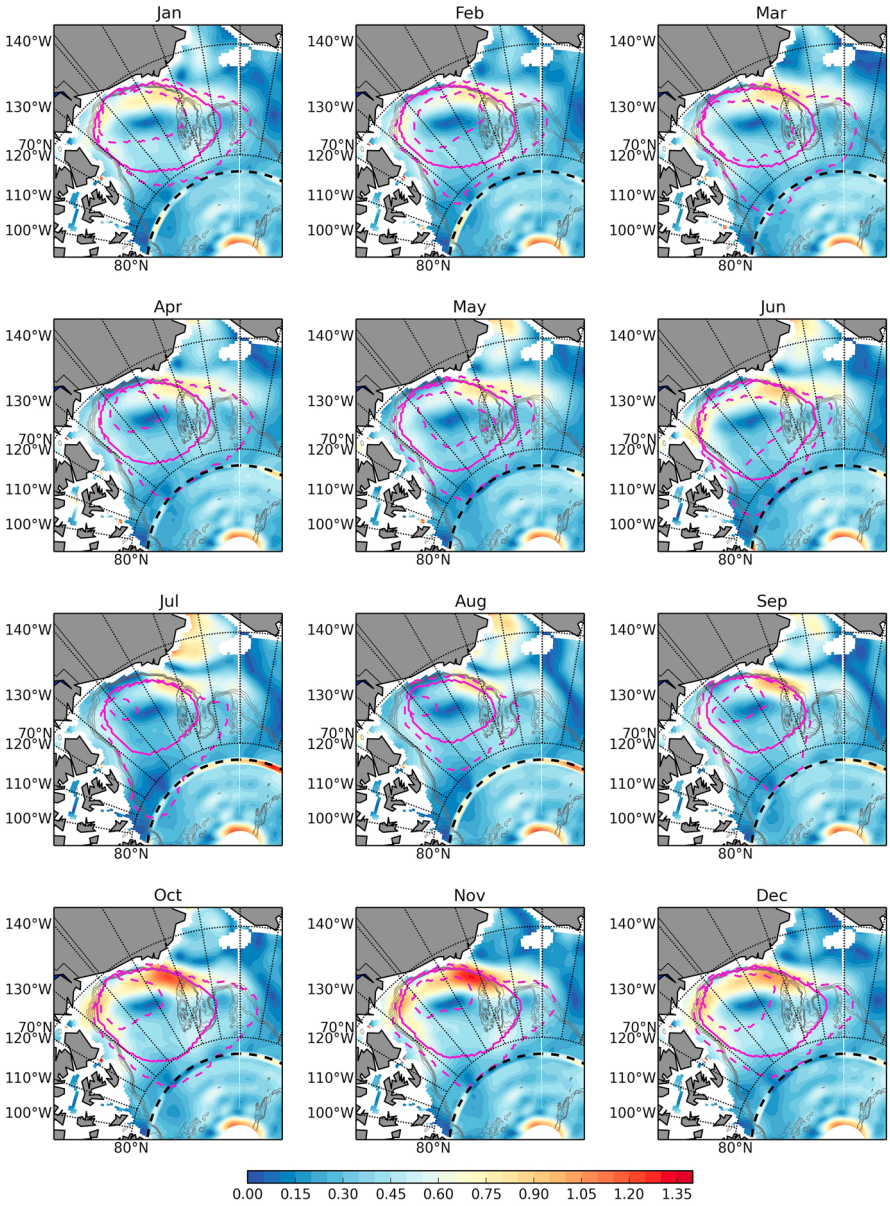

Figure 4. The magnitude of the lateral slope of dynamic ocean topography ($\times 10^6$ m elevation per lateral meters), displayed as monthly climatologies from 2003–2014. The 500, 1,000, and 1,500 m bathymetry contours are shown in gray, along with the gyre edge (magenta solid line). The minimum and maximum gyre area for each month are indicated by dotted lines. The northern limit of the dataset before 2011 is shown by a black dotted line.

(2016) and of BG freshwater content (Proshutinsky et al., 2009). Based on in situ observations, Proshutinsky et al. (2009) suggested that the June peak is attributable to salinity decrease resulting from sea ice melt, while the winter peak is due to increased thickness of the freshwater layer driven by elevated winter wind stress. Our analysis of the DOT fields reveals that the variations of the freshwater storage within the gyre can be linked with variations of both the gyre size and strength. Starting from August, when the gyre is the smallest, maximum DOT, strength, and area increase as BSH pressure increases from its August minima (Proshutinsky et al., 2002; Serreze & Barrett, 2011) and there is increased availability of freshwater from summer melting. The maximum strength and size are reached in October, at the end of the sea ice melting season. From October onwards, the maximum DOT decreases monotonically until it reaches a minimum in May, while the size of the gyre remains roughly constant. This is in contrast with the seasonal cycle of SLP over the region, which continues to increase until its maximum in March (Serreze & Barrett, 2011). One needs to remember, however, that the stress felt at the ocean surface is modulated by the presence of

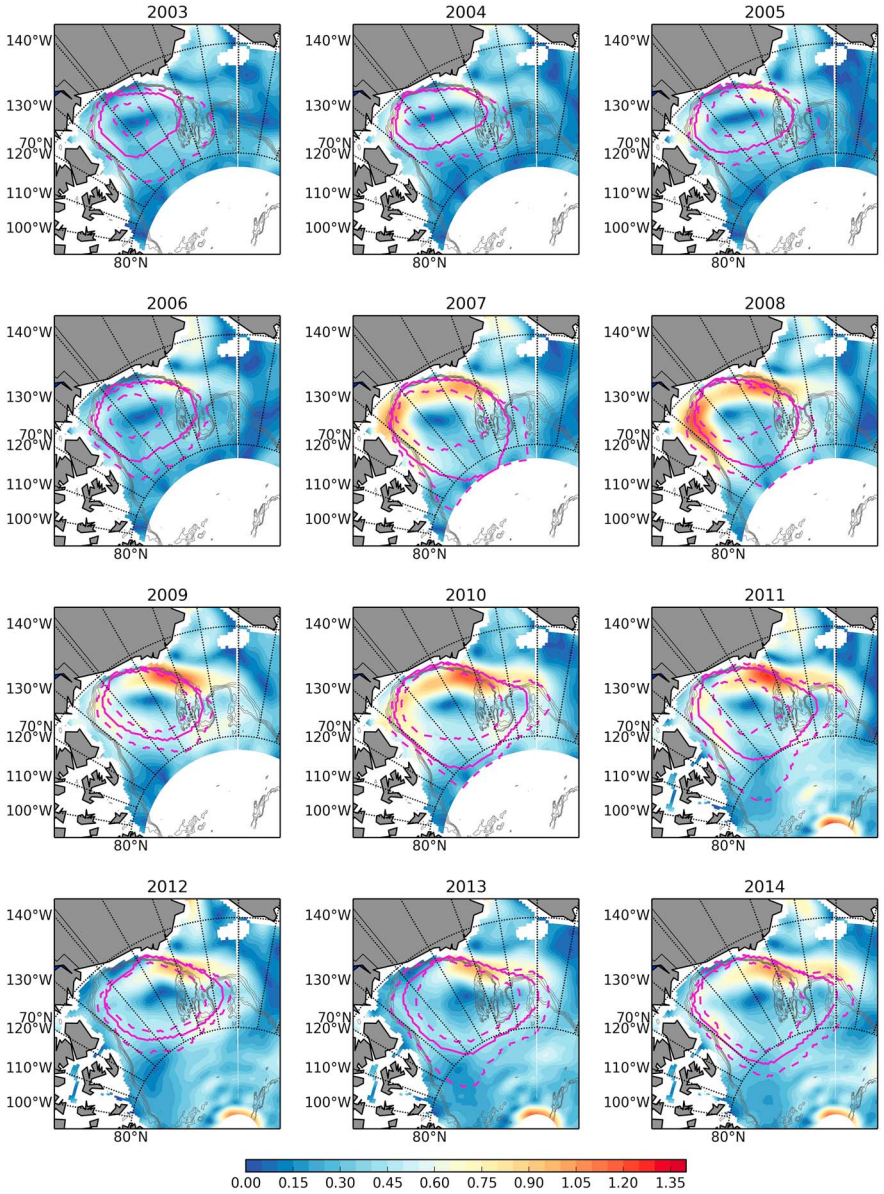

Figure 5. The magnitude of the lateral slope of dynamic ocean topography ($\times 10^6$ m elevation per lateral meters), displayed as annual averages. The 500, 1,000, and 1,500 m bathymetry contours are shown in gray, along with the gyre edge (magenta solid line). The minimum and maximum gyre area for each year are indicated by magenta dotted lines.

sea ice and in particular by the seasonal cycle of the sea ice thickness (Martin et al., 2016), which peaks in March–April, inhibiting the transmission of atmospheric momentum to the ocean and dampening the gyre's response to atmospheric forcing. In certain cases, surface geostrophic ocean velocities approach or exceed the sea ice drift, which reduces or reverses net Ekman pumping (Dewey et al., 2018; Meneghello, Marshall, Timmermans, & Scott, 2018; Zhong et al., 2018). In May–June, when a pulse of freshwater to the Arctic occurs due to thawing of land ice (Serreze et al., 2006) and river runoff (Peralta-Ferriz & Morison, 2010), the Canada Basin freshwater content increases. The maximum DOT appears to be more responsive to this increased availability of freshwater than the size of the gyre (explored further in section 4). From June to August, both the maximum DOT and the size of the gyre decrease, most likely as a response to the weaker winds.

3.2. Trends Over 2003–2014

Over the time period of 2003–2014, the area of the gyre increases, with a linear trend of 53,000 km^2/year (Figure 2c). The signal occurs alongside a shift in the location of the center (by 0.161°/year in latitude

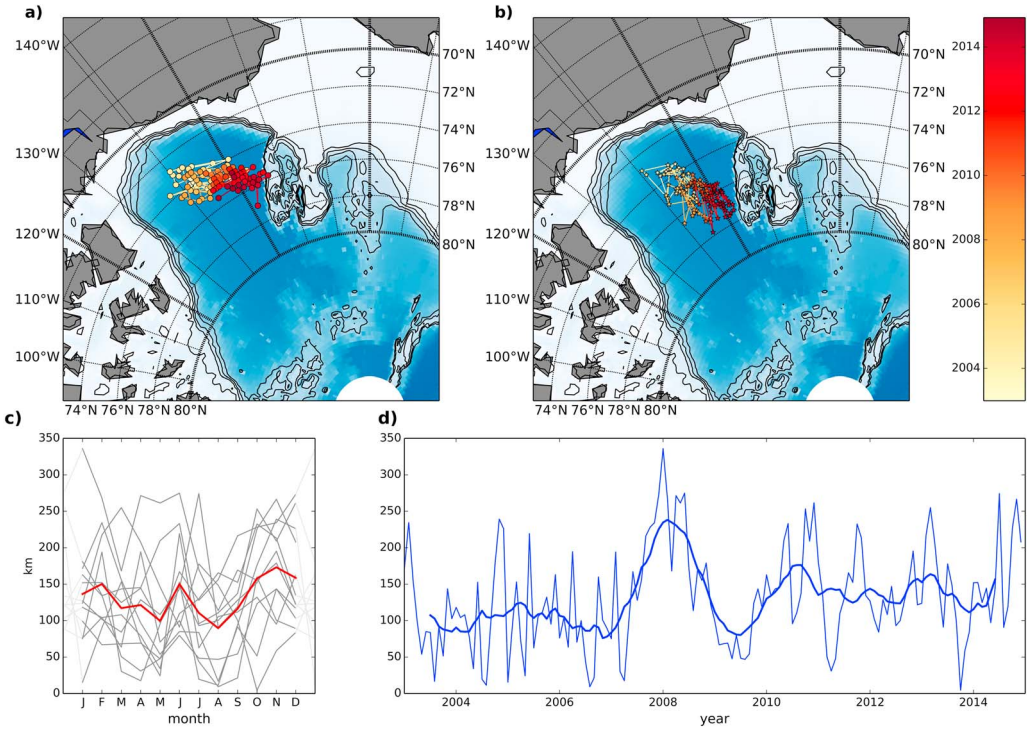

Figure 6. The location of (a) the maximum dynamic ocean topography and (b) the weighted center of the gyre for each month from 2003–2014, with successive months joined to show the trajectory over time. Also shown is (c) the seasonal cycle and (d) the interannual variability of the distance between the two centers.

and −0.821°/year in longitude, resulting in an average shift of 29.4 km/year along a bearing of 307.8°). It is accompanied by an overall increase of the maximum DOT (by 0.0138 m/year) and strength (by 0.0120 x 10^{-6}/year). Figure 7 shows the spatial structure of the linear trend of the DOT, calculated from a least squares approach. Although we only fit a linear trend, one needs to keep in mind that the trend might not be constant over time, with periods of plateauing or declining as seen in the maximum DOT (Figure 2a). This is consistent with plateauing of SSH after 2008 described by Zhang et al. (2016). The largest increase in the DOT field (with a trend of 0.0224 m/year) is found at 77.75°N, 159.75°W (Figure 7, black dot). This maximum is found west of the location of the gyre in 2003, in the region where the gyre has preferentially expanded. Our maximum trend is 128 km south of that found by Giles et al. (2012) over the time period 1995–2010 (Figure 7, cyan dot) but is also 0.0024 m/year larger, the difference being most likely due to the different period considered. It is 2–3 times smaller than the average DOT trend of 0.05–0.08 m/year in the Canada Basin over the shorter time period of 2005–2008 (Morison et al., 2012). Large trends are also found over the Northwind Ridge and Chukchi Plateau (Figure 7), reflecting the expansion of the gyre over that region. The intensification of the gyre, and its expansion and shift of its center away from the southeast and toward the northwest, result in an insignificant trend in DOT in the southeast where the gyre has resided almost continuously during 2003–2014.

The positive trend in DOT and expansion of the gyre (Figure 3) dominates the Arctic DOT trend and occurs in the context of an Arctic-wide freshening from 1992–2012 of 600 ± 300 km^3/year (Rabe et al., 2014), but the Arctic area-averaged 2005–2008 freshwater trend of 0.04 m/year (Morison et al., 2012) masks spatial variability in freshwater increase, particularly in the Canada Basin. Within this basin, Proshutinsky et al. (2009) detail 2003–2007 trends of freshwater at four locations as varying between 0.64 m/year (in the southeast of the gyre) and the maximum of 1.78 m/year at 78°N, 150°W, the furthest northwest location in their study, mimicking the trend in DOT. We speculate that, as the link between DOT and freshwater content is significant (e.g., Morison et al., 2012), the maximum trend in freshwater content continued to relocate further west after 2007, as per the DOT here. This trend of increasing DOT toward the west implies that the gyre deepens

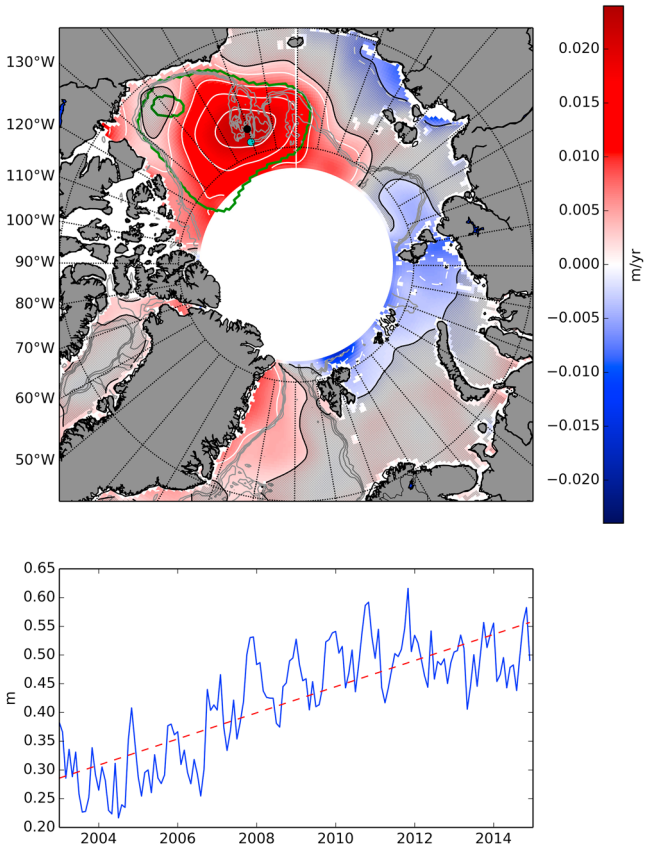

Figure 7. Map showing the linear trend (m/year) of the dynamic ocean topography time series at each location from 2003–2014. Time series of the dynamic ocean topography where the maximum trend occurs (black dot, over the Northwind Ridge) is shown below. The maximum trend found by Giles et al. (2012) is shown by a cyan dot. White contours indicate 0.005 m/year intervals, and areas which are not significant at the 95% level are hatched. The minimum and maximum gyre extent (in August 2004 and March 2013, respectively) are shown in green.

toward the Northwind Ridge and Chukchi Plateau (the latter being 300 m deep in places) from 2003–2014, increasing the interactions of the gyre with shallow bathymetry. Potential implications of this are discussed in section 4.

Rabe et al. (2014) apportion the 1992–2012 Arctic-wide freshening trend as two thirds due to salinity decrease and one third due to deepening of the halocline. Certainly, Armitage et al. (2016) find a dominance of steric height (and therefore density) change in the BG until 2011–2012, to be replaced by a dominance in the ocean mass component of the DOT field by the end of the time period. Within the BG a negative trend in sea ice thickness was observed in all seasons from 1980–2013 (Petty et al., 2016). However, Proshutinsky et al. (2009) found small positive trends of sea ice thickness within the gyre from 2003–2007 and suggest that, as a result, sea ice melt could only account for a maximum of 1 m/year freshening within the gyre. Similarly, in a study spanning 2004–2010, Krishfield et al. (2014) found that sea ice melting/freezing could account for up to 0.7 m of freshening each year, which is much smaller than the contribution from other sources. Armitage et al. (2016) suggested only a small portion of the freshening in the deep basins could be attributed to loss of freshwater from the Siberian shelves during this time period, equating to a shelf salinification of 0.15 psu/year, while Morison et al. (2012) identified a dipole behavior over 2005–2008, with a negative Eurasian Basin trend of 0.03–0.04 m/year offsetting the average DOT trend in the Canada Basin of 0.05–0.08 m/year. They propose that this is linked to a redistribution of freshwater between basins and thus increased availability of freshwater to the BG. Indeed, we find a small but significant reduction in DOT (the magnitude of which exceeds 0.005 m/year in places) along part of the continental shelf in the Eurasian Basin. A negative trend of this magnitude and areal extent was not observed by Giles et al. (2012) over 1995–2010. If advection from the Eurasian Basin is indeed a significant source to the BG, this finding suggests an intermittent, or increased, importance of this source in the 2000s and 2010s. Thus, the well-documented increase in freshwater content in the 2000s, which is evident in our observed trends in area and maximum DOT, appears to be predominantly due to additional input of freshwater by sources other than sea ice melt, despite yearly thinning of sea ice within the BG.

3.3. Interannual Variability

Superimposed on the long-term trend, the metrics of the gyre exhibit large interannual variations. When quantifying the interannual variations of the different fields, we do not remove a linear trend at each point before computation because in many parts of the gyre the change in DOT over time is nonlinear, displaying a similar rise and fall as the maximum DOT (Figure 2a, right panel) as the gyre expands asymmetrically and the center moves position. Where there is a large change in correlation between the full and detrended time series, we provide both values, and all correlations mentioned are significant at the 95% level. The standard deviations of the maximum DOT and the BG strength and size are of similar amplitude to that of their seasonal cycle, although the deviations of individual years from the mean seasonal cycle is large (Figure 2). Note that in several months the area is limited by the northern limit of the dataset, and therefore its value is slightly underestimated (magenta dots on Figure 2).

The years 2003–2007 display low interannual variability in both the maximum DOT and gyre strength, with the 12-month running mean of each for the first 4 years having an average standard deviation of 0.010 m and 0.021 x 10^{-6} respectively. The mean steric height of the BG from 2003 to the beginning of 2007 also showed little interannual variability (Armitage et al., 2016), suggesting that the eustatic component of DOT was also roughly constant during this time period. Over the course of 2007, the 12-month running mean of maximum DOT is raised from 0.50–0.63 m, reaching a maximum of 0.66 m in April of 2008 largely due to the peak DOT of 0.77 m that occurred in December 2007. The BG strength shows similar interannual

variability. Both remain high until 2012 when they drop to a local minimum in March 2013 before appearing to increase again, still remaining higher than 2003 values.

The gyre generally expands over time (Figures 2c, right panel, and 3b), but its southern and eastern edges are constrained by the presence of the Alaskan and Canadian coastlines and shallow bathymetry (Figure 3). Notably, the area increases before 2007, when the maximum DOT and strength are roughly constant (Figure 2, right panels). Therefore, the increase in freshwater content from the pre-1990s climatology that began before 2007 (Proshutinsky et al., 2009) manifested as an increase in area rather than a raise of maximum DOT. A similar expansion before raise in maximum DOT is seen after the drop of each metric in 2012. The interannual variability of the area correlates slightly better with strength (0.71) than with maximum DOT (0.67).

An increase in the rate of expansion is seen between 2007 and 2008, when the maximum DOT and strength raise, indicating a large increase in freshwater content within the gyre. This highlights that freshwater increase can manifest as both DOT change and gyre expansion, but the discrepancy between the two indicates that the maximum DOT and area could be controlled by different forcings and/or their timescale of response is different. This is particularly evident when noting that the maximum DOT remains high until 2012, while the area is reduced after 2008 until the end of 2010.

The interannual variations of the gyre area occur along with variations of the position of the center, although they correlate better with the changes of its latitude (correlation 0.61; Figure 2d, right panel) than longitude (correlation −0.35), suggesting some asymmetry developing as the gyre expands over time (Figure 3). Note here that the correlations drop to 0.29 and 0.12, respectively (the latter changing sign and becoming insignificant at the 95% level), when the linear trend is removed, indicating that the linear trend is a significant contributor to the correlation between area and location of the gyre center. The shrinking of the gyre in 2009, due to a reduced autumn-winter peak in size, coincides with a temporary westward shift of the eastern portion of the gyre, followed by a large shift to the west in 2010 (Figure 3b). The emergence of asymmetry is also visible from the increased distance between gyre center and centroid (which would match exactly in the case of a symmetrical gyre). Figure 6 highlights that these both begin in the Beaufort Sea and end by the Northwind Ridge, but their locations deviate over time, with the centroid shifting along an average trajectory of 325.3°. By December 2014, the centroid is 209 km almost directly north of the maximum DOT, with the 2014 average distance over 55% greater than that of 2003 (Figure 6). The asymmetry in the development of the gyre over time is also visible in Figure 5, where the gradient of the DOT tends to steepen more on the southwestern side of the gyre where the gyre is constrained by the presence of shallow bathymetry. This has been previously highlighted by Armitage et al. (2017), who found that, when the BG tends to expand, the geostrophic currents are intensified in both the southwest and southeast Beaufort Sea, where shallow bathymetric features are present.

Interannual variations of the BG strength (equation (1)) are mostly driven by the variations of the DOT at the gyre center (maximum DOT), with a correlation of 0.97 between the two 12-month running mean time series, as opposed to variation of the DOT at the edge (minimum DOT, correlation 0.64) or the average radius of the gyre (correlation 0.27). Moreover, the variations of the DOT at the center and edge of the gyre are not correlated. The edge DOT begins to raise during 2008 and reaches its peak in January 2010 (0.09 m greater than the minimum of maximum DOT in July 2004), 25 months after the peak in maximum DOT. After this, the DOT at the gyre edge lowers to pre-2008 levels.

In short, we have shown that the different characteristics of the BG exhibit large seasonal, interannual, and long-term variability. Seasonally, the gyre undergoes a strong weakening in summer, which manifests itself as reduced maximum DOT, strength, and area, the latter roughly halving in July–September compared to the rest of the year. Two peaks in the seasonal cycle of maximum DOT agree well with observations of freshwater content within the gyre. Over the period of 2003–2014, the gyre expands at a rate of 53,000 km/year, toward the north and west, with an asymmetry developing after its western edge resides over the Chukchi Plateau

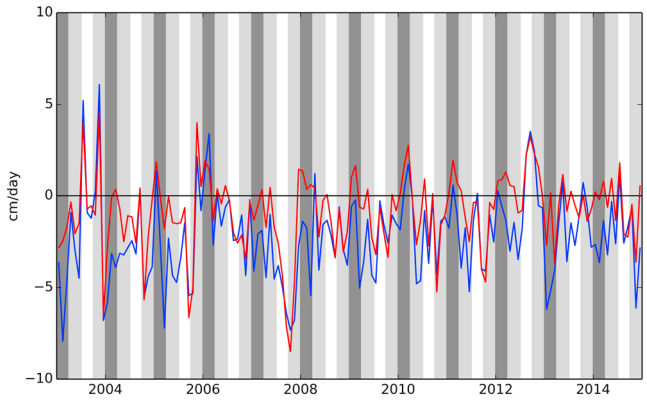

Figure 8. Time series of the average Ekman upwelling (cm/day) as predicted by considering only the atmospheric forcing (blue) and the total surface stress on the ocean (red) within the BG box (70.5–80.5°N, 190–230°E; Proshutinsky et al., 2009; black box in Figure 1) from 2003–2014. Dark gray highlights winter (January–March), while light gray highlights spring (April–June) and autumn (October–December).

year-round. The maximum DOT and strength are raised between 2007 and 2012 but then fall (remaining above pre-2007 levels), highlighting a decoupling between variations in the size and strength of the gyre.

4. Atmospheric Forcing and Other Controls on the Gyre

Here we put the spatial and temporal behavior of the key gyre metrics in the context of the atmospheric forcing, in order to investigate the gyre's response. Due to the uncertainty surrounding the specific role of the sea ice in modulating the momentum input from the wind to the ocean surface, we look at both the effect of the wind forcing only, neglecting the presence of sea ice, and also consider the surface stress when including the effects of sea ice and surface geostrophic currents. We then describe the role played by the bathymetry of the Canada Basin in modulating the response of the gyre to its surface forcing and discuss the implications of our findings on freshwater content and observations.

4.1. Atmospheric Forcing

We look at both the intensity of the atmospheric forcing and the position of the BSH (Beaufort Sea High) in order to understand their separate and combined effects on the gyre metrics. We use the SLP field to determine the position of the BSH, noting that its center generally aligns well with the wind stress curl maximum (not shown), and we compute the Ekman pumping within the BG box to investigate the effect of the forcing on the gyre. We use the BG box here, rather than within the contour-defined gyre, for two reasons. The first is that the use of the same, or similar, boxes in the literature (e.g., Krishfield et al., 2014; Meneghello, Marshall, Timmermans, & Scott, 2018; Proshutinsky et al., 2009) allows comparisons to be made with this study. The second is that the gyre has some memory of the forcing (Johnson et al., 2018), which implies some lag in its response, and so it is difficult to make direct comparisons between the forcing just over the closed contour and the gyre metrics for any given month.

The two computations of average Ekman pumping from total surface stress (equation (2)) and wind-only surface stress (equation (2), $\alpha = 0$) within the BG box over time (Figure 8) are well correlated (0.81 with the daily stress). Here we do not detrend so that we remain consistent with the gyre metrics, but the forcing time series do not contain a notable linear trend. A difference in magnitude but not temporal variability is observed, and downwelling is reduced, or altered to weak upwelling, when including ice-ocean stress, τ_{ice}, in the Ekman pumping calculation (equation (5)). This is particularly evident in winter where upwelling (recently described by Dewey et al., 2018, and Meneghello, Marshall, Timmermans, & Scott, 2018) follows a downwelling peak in September–October in all but a few years. These different years, 2003, 2012, and 2013, display no increase in summer downwelling, with 2012 instead showing increased winter downwelling and sustained summer-autumn upwelling when the Arctic experienced the strongest summer cyclone since records began in 1979 (Simmonds & Rudeva, 2012). They are aligned with, or follow, low annual average SLP across the Canada Basin (Figure 9) and coincide with low gyre extent and maximum DOT. Conversely, the largest downwelling is seen in 2007 (Figure 8), when SLP is anomalously high during summer and autumn and the magnitude of the total Ekman pumping exceeds the wind-only forcing for 2 months. This coincides with a significant increase in maximum DOT, strength, and area, when anomalous wind conditions contributed to a significant retreat of sea ice (Zhang et al., 2008) and a large increase in ice-free area around the BG compared to 2006 (Petty et al., 2016). Thus, 2007 and 2012 exhibit the strongest anomalies in the forcing over 2003–2014, when we also observe the strongest changes in DOT.

The gyre characteristics display a trend (Figure 7 and section 3.2), while the forcing does not, which results in lower correlations between the fields than if they were detrended; however, some significant correlation is still present. The strongest correlation between gyre characteristics and Ekman pumping is found with the gyre strength, but it is low at 0.19. It increases to 0.33 when correlating the gyre strength to the Ekman pumping of the previous month, suggesting a lag in response. Notably, this increases further to 0.43 (0.61 if removing a linear trend from each) when considering the gyre strength and the average Ekman pumping over the previous 3 months and 0.44 if also including the present month. Similarly, Dewey et al. (2017) found

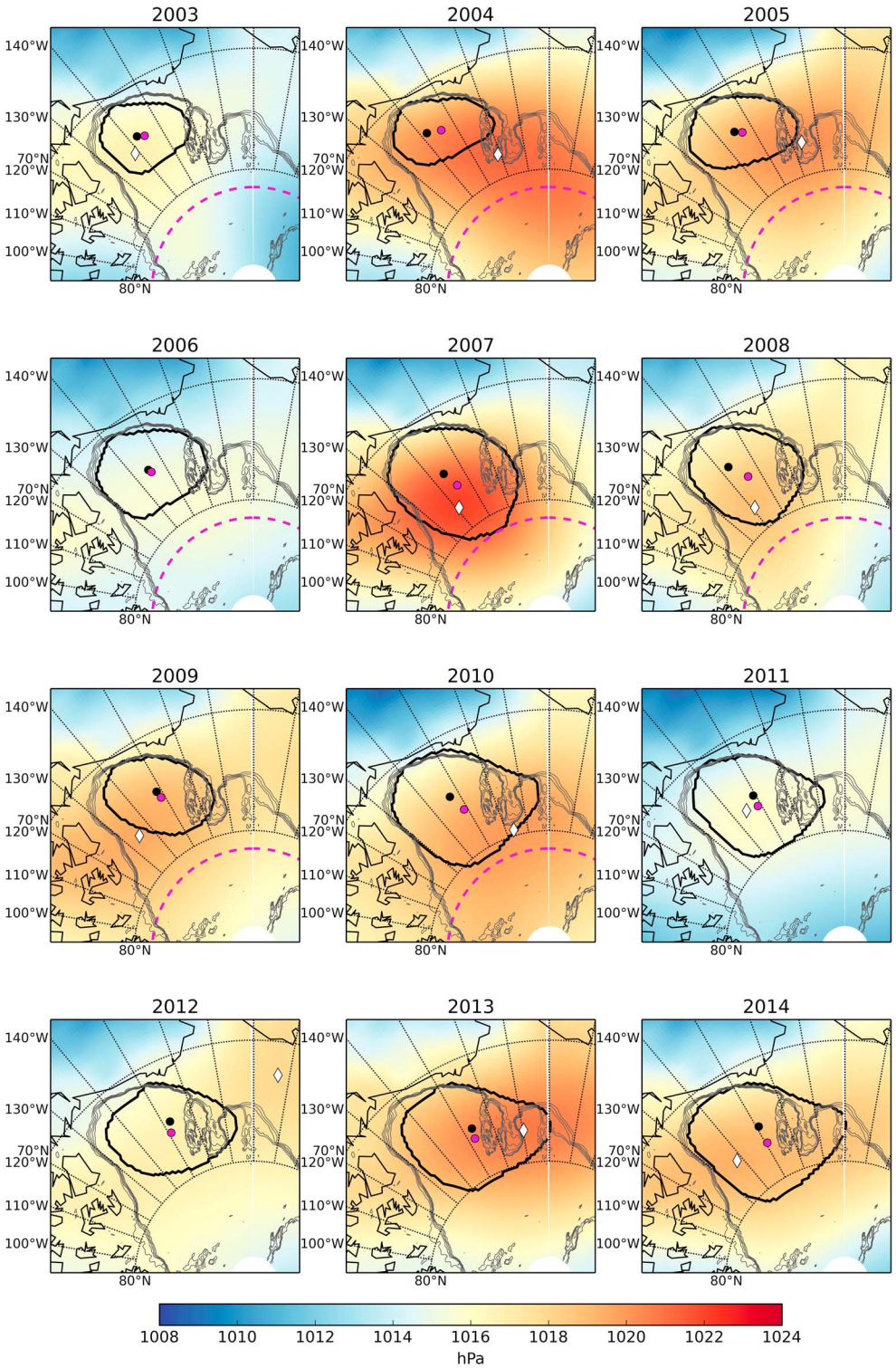

Figure 9. Annual sea level pressure (SLP) over the Beaufort Gyre, with gyre edge outlined in black. Location of maximum dynamic ocean topography (black) and weighted center of gyre (magenta) are shown, along with location of maximum SLP (white diamond). Also shown in gray are the 500, 1,000, and 1,500 m isobaths. The northern limit of the 2003–2010 dataset is highlighted (magenta dotted line). Note that in 2006 the maximum SLP lies to the southeast of the region shown.

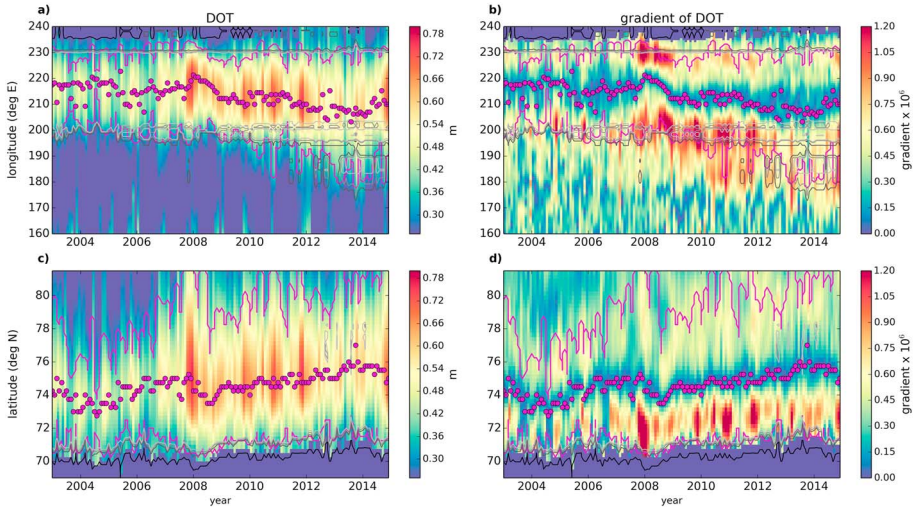

Figure 10. Hovmöller plots through the center of the gyre over time. Sections through the latitude of the center in each month (a, b) and through the longitude of the center in each month (c, d) are shown for (a, c) dynamic ocean topography (DOT) and (b, d) the magnitude of its spatial gradient ($\times 10^6$ m elevation per lateral meters). Magenta dots/lines show the position of the maximum DOT and gyre edge. Bathymetry contours shown at 500 (black), 1,000 (gray), and 1,500 m (light gray). It is important to note that, as the gyre center moves from 2003–2014 (Figure 6), the section of DOT taken varies, and thus, the bathymetry contours do not necessarily represent the same features over time.

a 2-month lag between the Arctic Oscillation index and salinity distribution (and thus gyre doming) along 150°W within the gyre from 2012–2014, suggesting some memory of the forcing. The effect of sea ice cover on the magnitude of the total surface stress is not strong in spring and autumn compared to the winter, with reduced sea ice thickness and extent allowing for more transfer of momentum from the wind.

We suggest that both the position and the intensity of the forcing are important in determining the size and shape of the gyre, and the gyre's overall location is affected by the movement of the BSH. Figure 9 shows that if the intensity of the BSH is strong, but its center is to the east of the gyre, the gyre is likely to remain smaller than if it were to the west. Conversely, a western located SLP can result in a gyre expansion to the west even if the intensity has not greatly increased (Figure 9, 2007 compared to 2010). In 2004, 2005, 2010, 2012, and 2013, the center of the BSH is to the west of the gyre center, and the western portion extends over the Chukchi Plateau. It should also be noted that the gyre shrinks in summer, when the BSH position is generally to the east (not shown). In 2007 and 2010, the gyre expands northward toward the average location of the BSH. From 2010 onwards, the western edge of the gyre remains to the west of the Chukchi Plateau despite the average location of the center of the BSH in 2011 and 2014 occurring to the east of the gyre center. The fact that 2004 and 2005 have a westward BSH center but the gyre in these years remains small points to further controls on the gyre size and shape.

4.2. Bathymetric Controls

The location and strength of the BSH, and the resulting surface stress when including the effect of sea ice, cannot fully predict the gyre behavior. The winter location of the BSH is regularly to the west of the BG (Figure 9), but the gyre position does not grow directly toward the center of the BSH. Here we point to bathymetry as being a significant, previously overlooked control on the gyre dynamics. Yang et al. (2016) have suggested that a meridional ridge could act to mimic a western boundary for the gyre in the absence of a western land barrier to create a western boundary current. The Chukchi Plateau region has been identified as an area of disturbed currents at the gyre edge (Armitage et al., 2017) and increased eddy density (Zhao et al., 2016), suggesting that there is some interaction between gyre circulation and subsurface topography.

Figure 10 shows the DOT field and its gradient along the latitude and longitude of the maximum DOT, therefore providing an indication of its behavior along the "central" axis. Note the moving center means that the bathymetry encountered also varies over time. The BG experiences resistance when it expands toward shallow bathymetry (Figure 10), as indicated by the increased DOT gradient along the continental slope (Figure 5; Armitage et al., 2017). The southwestern edge of the gyre never breaches the continental shelf of

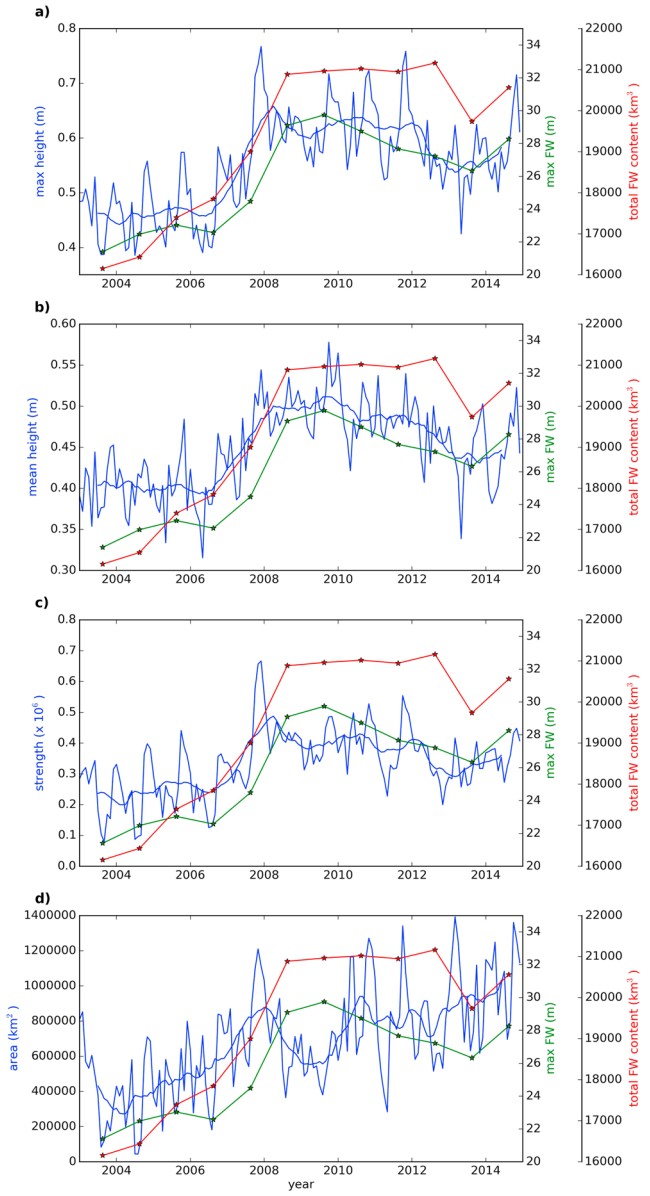

Figure 11. Time series showing (a) maximum dynamic ocean topography (DOT), (b) mean DOT within the gyre, (c) strength ($\times 10^6$), and (d) area of the gyre, along with their 12-month running means (blue). Maximum freshwater (FW) content during the summer of each year (Beaufort Gyre Exploration Project; Proshutinsky et al., 2009, updated each year) is shown in green, while total summer FW content within the BG box (Figure 1, black box; Proshutinsky et al., 2009) is show in red. Note that the FW content lines are plotted in August of each year.

the Chukchi Sea shallower than 200 m. While the theoretical Ekman effect only reaches the upper tens of meters, the gyre is also constrained by the Atlantic Water boundary current that flows along f/H contours (e.g., Lique et al., 2015) or the current flowing on the shelf break (Pickart et al., 2013). Thus, the underlying water residing between the gyre and the sea bed, which is directly impacted by shallow bathymetry, affects the overlying gyre by its presence. The Northwind Ridge, exceeding 700 m, does not create a significant limitation for the gyre, but the adjacent Chukchi Plateau (encountered consistently after 2008, albeit at varying latitudes) creates a northward extension from the Chukchi Sea shelf, which is shallower than 300 m in places. Note that the Chukchi Plateau is a strong downwelling region (Meneghello, Marshall, Timmermans, & Scott, 2018; Timmermans et al., 2014), particularly from September to December when the gyre is expanding. The bathymetric control goes some way to explaining the original finding by Giles et al. (2012) that the gyre expanded to the northwest over 1995–2010 but the center did not significantly shift position.

The three-dimensional structure of the gyre can be inferred from a steepened DOT gradient, which indicates steepened isopycnals. Over shallow bathymetry, the steepened isopycnals will tend to interact with (and thus be constrained by) the bathymetric feature and likely also with the Atlantic Water boundary current (e.g., Lique & Johnson 2015). This current circulates cyclonically around the continental slope of the Arctic Basin; while meandering around the Chukchi Plateau, there is development of an additional branch flowing into the interior of the ocean (Aksenov et al., 2011; McLaughlin et al., 2009; Woodgate et al., 2007), with a weaker branch also transiting through the Chukchi Gap at the base of the Chukchi Plateau (McLaughlin et al., 2004, 2009), over which the gyre lies consistently from 2010 onward. The raised DOT in 2008 results in a steeper gradient along each of the southern, eastern, and western bounds (Figure 5). After 2009 this extends westward, consistently breaching the Chukchi Plateau after 2012, and in 2013 the western edge of the gyre is aligned with the Mendeleev Ridge. In its new position, the DOT reduces, which we suggest is partially due to a relaxation of the gyre as it is able to expand over the plateau more easily and the isopycnals below flatten (Figure 10). We speculate that this behavior represents the bathymetric constraint of the shallow Chukchi Plateau limiting the gyre expansion, thus causing the gradient to increase until some threshold is reached, after which it is able to breach the western limit and expand more freely, which we observe in our data (Figure 3b). The proposed increased interaction with the bathymetry is likely to result in more instabilities, which may be linked to the intensified eddy activity observed by Zhao et al. (2016) during 2013–2014 close to the Chukchi Plateau. The Mendeleev Ridge generally exceeds 1,500-m depth, which would likely cause less of a restriction on the gyre than the proposed constraint caused by the Chukchi Plateau. Indeed, the latter still appears to have an effect on the gyre after the western portion expands beyond it, with the weighted center deviating more from the maximum DOT due to continued asymmetry. The expansion of the gyre to reside over the Chukchi Plateau year-round is likely to lead to a new dynamical equilibrium being established as the gyre responds to the shallow bathymetry.

4.3. Implications for Freshwater Content Variability and Its Observability

In order to relate our findings to gyre freshwater content variations, we compare the gyre parameters to summer freshwater variations, in terms of both the maximum freshwater content within the gyre and the total freshwater content within the BG box (Proshutinsky et al., 2009) in Figure 11. We use the BG box here,

because the yearly BGEP gridded data are interpolated from CTD profiles from July to October of each year (Proshutinsky et al., 2009), and therefore it is meaningless to analyze the data within the closed contour of a particular month, or yearly average contour, given that the data are not from a specific month and do not include winter.

We reiterate here that freshwater change within the gyre can be reflected by both a change in maximum DOT and the area of the gyre, but their variations are not always in phase. The total freshwater content is mirrored by the 12-month running mean of maximum DOT, with a peak in 2008, followed by a plateau until 2012 when both fields decrease before beginning to increase again in 2014. This similarity in interannual variations shows that the maximum DOT is a good predictor of summer freshwater behavior. The maximum freshwater content, which we might expect to display similar interannual variations to that of maximum DOT, instead shows more similarity to the mean height across the gyre and declines after 2009, suggesting a redistribution of freshwater within the gyre following the anomalously anticyclonic atmospheric conditions during 2007.

The area of the gyre closely follows the behavior of freshwater content from 2003–2008, both increasing while maximum DOT, mean DOT, and strength remain roughly constant, suggesting that during these years the main signature of increased freshwater content within the gyre is expansion. Notably, the drop in gyre strength and area in 2009 is not reflected in either the maximum or total freshwater content. As we compute the total freshwater content over the BG box, the computation does not take into account the change in gyre size. If we assume the data were collected in August and compare the gyre area in this month to the freshwater content within this closed contour, the interannual variability of the gyre area agrees well (not shown). We suggest that the finding that the maximum freshwater content, which is independent of the chosen computation region, does not drop in 2009 is evidence that the freshwater content during this year manifests more as elevated mean DOT than areal extent. We propose that this is because the bathymetric constraint limits expansion to the west, somewhat counteracting the effect of the forcing. As a larger portion of the gyre eventually breaches over the Chukchi Plateau in 2012–2014, the intensity of the gyre relaxes, corresponding to a temporary drop in total freshwater content before all fields begin to rise in the last year of the period studied.

The region defined first by Proshutinsky et al. (2009) captures the majority of the gyre, including in years where the expansion to the north and west is large. Additionally, the surface forcing within the bounds of the BG box (Proshutinsky et al., 2009) and within the BG area computed in this study have high correlation (0.89 and 0.87 for Ekman pumping from wind-only and total surface stress computations, respectively). Mooring sites of the BGEP are also contained within the gyre for most of the time period considered. It should be noted that, as the gyre shifts position, its center moves toward moorings A and B of the BGEP (Proshutinsky et al., 2009; shown in Figure 1). Therefore, while overall gyre freshwater content within the gyre increased during the 2000s (e.g., Armitage et al., 2016; Krishfield et al., 2014), the increases in freshwater observed at the moorings were likely partially due to the reduced distance from the moorings to the gyre center. Expansion of the gyre and relocation of its center must therefore be considered when interpreting discrete measurements and inferring gyre-wide change.

Increased freshwater content and spin-up of the gyre occurs alongside a deepening of the underlying Atlantic Water toward the Northwind Ridge of over 100 m in 2003–2011 (Zhong & Zhao, 2014), which corresponds well with the BG center migration observed in this study. This increased depth of the Atlantic Water layer below the BG was attributed to cooling of the layer but could also be a response to increased freshwater content and depth of the BG. Lique et al. (2015) found that Atlantic Water was affected by changes to the surface circulation, suggesting a potential for further-reaching effects as the Atlantic Water layer below will deepen and likely be restricted near the shelf by an intensified gyre.

Variations of the gyre may affect other features within the Canada Basin. Woodgate (2018) finds an increase in transport of Pacific Water through the Bering Strait into the Arctic from 1990–2015. During the time period of this study, the years of anomalously high annual mean inflow of the fresh Pacific Water are generally followed by an increase in gyre size in all but one year. Additionally, it is known that fluxes of heat, freshwater, and nutrients into the Canada Basin from the Alaskan portion of the Beaufort Sea are affected by an eastward shelf break jet and storm events (Pickart et al., 2013). While the pathways and destination of water off of the shelves are not fully constrained, the increased proximity of the gyre to the shelf break of the Beaufort and Chukchi seas, which is reached year-round after 2009, could increase interactions between the gyre

and shelf or serve to disrupt the eastward shelf break jets that prevail. Increased access to the Chukchi Sea is particularly important given that it experienced freshening in winter 1990–2015 (0.03 psu/year) and warming in May and June due to earlier arrival of warmer water (Woodgate, 2018). In addition to exchanges with the shelf, basin-wide changes to freshwater pathways seen in the mid-2000s (Morison et al., 2012) could both have fueled an expanded gyre and have been affected in their trajectories, thus potentially having increasing interaction and impact on flow from the Eurasian Basin and out of the Arctic Ocean. Further work must be done on the impact of the changes to the gyre highlighted in this study and their effects on the surrounding region, so that the nonlocal effects of change to freshwater content and gyre forcing can be understood.

5. Conclusions

In this study, we have used altimetry-derived DOT to describe the monthly evolution of the shape, size, and location of the BG within the Canada Basin. We conclude that the gyre expanded between 2003 and 2014, in line with freshwater content over the majority of the period (Armitage et al., 2016; Krishfield et al., 2014) and despite a reduced maximum DOT in 2013–2014.

Among the detailed description of the gyre, we draw attention to three key findings. The first is that, as for steric height (Armitage et al., 2016), the maximum DOT of the gyre displays similar seasonality to measured freshwater content (Proshutinsky et al., 2009) despite temporal and spatial differences. However, the best metric for describing the gyre response to surface forcing is the gyre strength, which also includes the response of the minimum DOT within the gyre and its average radius. The gyre responds to the cumulative effect of forcing, with the strongest correlation being found over the previous 3 months of forcing. This highlights memory of the gyre, which has also been proposed to exist on decadal timescales by Johnson et al. (2018). This means that during 2007 and 2012, when the gyre experienced anomalous forcing throughout the year, the BG displayed the largest response to the surface forcing. That these 2 years had the lowest sea ice across 2003–2014 suggests increased sensitivity of the gyre to extreme events, and thus, the continuing summer decline of sea ice within the BG may have implications for future gyre behavior.

The second important result is that the maximum DOT and area of the gyre do not linearly covary, either seasonally or interannually. While the maximum DOT responds well to the intensity of the surface forcing, the gyre size additionally depends on the location of the BSH. Thus, in the summer, when the BSH is generally to the east, the gyre area halves, while for the rest of the year it remains roughly constant while maximum DOT sees a decline in spring and additional peak in June. A similar control is observed in the longer term behavior, hence the decoupling. Over 2003–2014, the freshwater content variations manifest as both changes to the size of the gyre and the maximum DOT, but not necessarily at the same time.

Finally, we note that the fact that the areal extent of the gyre is forced by the position, as well as magnitude, of the BSH, means that when the BSH resides to the west of the Chukchi Plateau, its shallow bathymetry impedes movement of the gyre, resulting in asymmetry. This is emphasized by the deviation of the maximum DOT and weighted center of the gyre, and strong correlation between maximum DOT and gradient at the western limit of the gyre. Some relaxation in gradient after a breach over the Chukchi Plateau (to become realigned with the Mendeleev Ridge) suggests a new western boundary is reached, although further analysis beyond 2014 is required to deduce whether this is a temporary relocation or a new geographical position for the BG. We highlight the potential importance of the proximity of freshwater sources from the Chukchi Sea, altered seasonality of the gyre, and effect of shallow bathymetry on the western limbs of the gyre and its underlying water masses as questions to focus on in the future. The effect of these factors will be further elucidated by the future availability of longer time series at higher resolution and greater spatial coverage.

Overall, our study emphasizes the importance of the bathymetry for the dynamics of the gyre and reveals that both the variations of the location and intensity of the atmospheric forcing play a role for the variations of the BG intensity and area (and thus the associated freshwater content variations). To date, idealized process models probing the dynamics at play for the BG (Davis et al., 2014; Lique et al., 2015; Manucharyan et al., 2016) have largely overlooked these factors, and their effects should be included in future studies.

Acknowledgments
H. Regan and C. Lique acknowledge support from Ifremer, Région Bretagne and the INSU/LEFE program through the funding of project FREDY. T. Armitage was supported at the Jet Propulsion Laboratory, California Institute of Technology, under a contract with the National Aeronautics and Space Administration. We acknowledge valuable discussions initiated by the Forum for Arctic Modeling and Observational Synthesis (FAMOS) Project. In particular, we are grateful for insightful discussions with Helen Johnson and Gianluca Meneghello, who provided useful input into the direction of the analysis for this paper. The freshwater content data were collected and made available by the Beaufort Gyre Exploration Program based at the Woods Hole Oceanographic Institution (http://www.whoi.edu/beaufortgyre) in collaboration with researchers from Fisheries and Oceans Canada at the Institute of Ocean Sciences. Arctic dynamic topography/geostrophic currents data were provided by the Centre for Polar Observation and Modelling, University College London (www.cpom.ucl.ac.uk/dynamic_topography) (Armitage et al., 2016, 2017).

References

Aagaard, K., & Carmack, E. (1989). The role of sea ice and other fresh water in the Arctic circulation. *Journal of Geophysical Research*, *94*, 14,485–14,498.

Aksenov, Y., Ivanov, V. V., Nurser, A. J. G., Bacon, S., Polyakov, I. V., Coward, A., et al. (2011). The Arctic Circumpolar Boundary Current. *Journal of Geophysical Research*, *116*, C09017. https://doi.org/10.1029/2010JC006637

Armitage, T. W. K., Bacon, S., Ridout, A. L., Petty, A. A., Wolbach, S., & Tsamados, M. (2017). Arctic Ocean surface geostrophic circulation 2003–2014. *The Cryosphere*, *11*, 1767–1780. https://doi.org/10.5194/tc-11-1767-2017

Armitage, T. W. K., Bacon, S., Ridout, A. L., Thomas, S., Aksenov, Y., & Wingham, D. J. (2016). Arctic sea surface height variability and change from satellite radar altimetry and GRACE, 2003–2014. *Journal of Geophysical Research: Oceans*, *121*, 4303–4322. https://doi.org/10.1002/2015JC011579

Belkin, I. M. (2004). Propagation of the "Great Salinity Anomaly" of the 1990s around the northern North Atlantic. *Geophysical Research Letters*, *31*, L08306. https://doi.org/10.1029/2003GL019334

Belkin, I. M., Levitus, S., Antonov, J., & Malmberg, S.-A. (1998). "Great Salinity Anomalies" in the North Atlantic. *Progress in Oceanography*, *41*, 1–68.

Broecker, W. S. (1997). Thermohaline circulation, the achilles heel of our climate system: Will man-made CO_2 upset the current balance? *Science*, *278*, 1582–8.

Carmack, E. C., Yamamoto-Kawai, M., Haine, T. W. N., Bacon, S., Bluhm, B. A., Lique, C., et al. (2016). Freshwater and its role in the Arctic Marine System: Sources, disposition, storage, export, and physical and biogeochemical consequences in the Arctic and global oceans. *Journal of Geophysical Research: Biogeosciences*, *121*, 675–717. https://doi.org/10.1002/2015JG003140

Comiso, J. C. (2017). Bootstrap sea ice concentrations from Nimbus-7 SMMR and DMSP SSM/I-SSMIS, Version 3 (Northern Hemisphere). Boulder, CO: NASA National Snow and Ice Data Center Distributed Active Archive Center. https://doi.org/10.5067/7Q8HCCWS4I0R

Coupel, P., Ruiz-Pino, D., Sicre, M.-A., Chen, J. F., Lee, S. H., Schiffrine, N., et al. (2015). The impact of freshening on phytoplankton production in the Pacific Arctic Ocean. *Progress in Oceanography*, *131*, 113–125.

Danielson, S. L., Weingartner, T. J., Hedstrom, K. S., Aagaard, K., Woodgate, R., Curchitser, E., & Stabeno, P. J. (2014). Coupled wind-forced controls of the Bering-Chukchi shelf circulation and the Bering Strait throughflow: Ekman transport, continental shelf waves, and variations of the Pacific-Arctic sea surface height gradient. *Progress in Oceanography*, *125*, 40–61.

Davis, P. E. D., Lique, C., & Johnson, H. L. (2014). On the link between Arctic sea ice decline and the freshwater content of the Beaufort Gyre: Insights from a simple process model. *Journal of Climate*, *27*, 8170–8184. https://doi.org/10.1175/JCLI-D-14-00090.1

Dee, D. P., Uppala, S. M., Simmons, A. J., Berrisford, P., Poli, P., Kobayashi, S., et al. (2011). The ERA-Interim reanalysis: Configuration and performance of the data assimilation system. *Quarterly Journal of the Royal Meteorological Society*, *137*(656), 553–597. https://doi.org/10.1002/qj.828

Dewey, S., Morison, J., Kwok, R., Dickinson, S., Morison, D., & Andersen, R. (2018). Arctic ice-ocean coupling and gyre equilibration observed with remote sensing. *Geophysical Research Letters*, *45*, 1499–1508. https://doi.org/10.1002/2017GL076229

Dewey, S., Morison, J., & Zhang, J. (2017). An edge-referenced surface fresh layer in the Beaufort Sea seasonal ice zone. *Journal of Physical Oceanography*, *47*, 1125–1144.

Dickson, R. R., Meincke, J., Malmberg, S.-A., & Lee, A. J. (1988). The "great salinity anomaly" in the northern North Atlantic 1968–1982. *Progress in Oceanography*, *20*, 103–151.

Foukal, N., & Lozier, M. (2017). Assessing variability in the size and strength of the North Atlantic subpolar gyre. *Journal of Geophysical Research: Oceans*, *122*, 6295–6308. https://doi.org/10.1002/2017JC012798

Giles, K. A., Laxon, S. W., Ridout, A. L., Wingham, D. J., & Bacon, S. (2012). Western Arctic Ocean freshwater storage increased by wind-driven spin-up of the Beaufort Gyre. *Nature Geoscience*, *5*, 194–197. https://doi.org/10.1038/ngeo1379

Haine, T. W. N., Curry, B., Gerdes, R., Hansen, E., Karcher, M., Lee, C., et al. (2015). Arctic freshwater export: Status, mechanisms, and prospects. *Global and Planetary Change*, *125*, 13–35. https://doi.org/10.1016/j.gloplacha.2014.11.013

Häkkinen, S., & Rhines, P. B. (2004). Decline of subpolar North Atlantic circulation during the 1990s. *Science*, *304*, 555–559.

Jahn, A., & Holland, M. M. (2013). Implications of Arctic sea ice changes for North Atlantic deep convection and the meridional overturning circulation in CCSM4-CMIP5 simulations. *Geophysical Research Letters*, *40*, 1206–1211. https://doi.org/10.1002/grl.50183

Johnson, H. L., Cornish, S., Kastov, Y., Beer, E., & Lique, C. (2018). Arctic Ocean freshwater content and its decadal memory of sea-level pressure. *Geophysical Research Letters*, *45*, 4529–5228. https://doi.org/10.1029/2017GL076870

Karcher, M., Gerdes, R., Kauker, F., Köberle, C., & Yashayaev, I. (2005). Arctic Ocean change heralds North Atlantic freshening. *Geophysical Research Letters*, *32*, L21606. https://doi.org/10.1029/2005GL023861

Krishfield, R. A., Proshutinsky, A., Tateyama, K., Williams, W. J., Carmack, E. C., McLaughlin, F. A., & Timmermans, M.-J. (2014). Deterioration of perennial sea ice in the Beaufort Gyre from 2003 to 2012 and its impact on the oceanic freshwater cycle. *Journal of Geophysical Research: Oceans*, *119*, 1271–1305. https://doi.org/10.1002/2013JC008999

Lique, C., & Johnson, H. L. (2015). Is there any imprint of the wind variability on the Atlantic Water circulation within the Arctic Basin? *Geophysical Research Letters*, *42*, 9880–9888. https://doi.org/10.1002/2015GL066141

Lique, C., Johnson, H. L., & Davis, P. E. D. (2015). On the interplay between the circulation in the surface and the intermediate layers of the Arctic Ocean. *Journal of Physical Oceanography*, *45*, 1393–1409. https://doi.org/10.1175/JPO-D-14-0183.1

Lique, C., Treguier, A.-M., Scheinert, M., & Penduff, T. (2009). A model-based study of ice and freshwater transport variability along both sides of Greenland. *Climate Dynamics*, *33*, 685–705.

Ma, B., Steele, M., & Lee, C. (2017). Ekman circulation in the Arctic Ocean: Beyond the Beaufort Gyre. *Journal of Geophysical Research: Oceans*, *122*, 3358–3374. https://doi.org/10.1002/2016JC012624

Manucharyan, G. E., & Spall, M. A. (2016). Wind-driven freshwater buildup and release in the Beaufort Gyre constrained by mesoscale eddies. *Geophysical Research Letters*, *43*, 273–282. https://doi.org/10.1002/2015GL065957

Manucharyan, G. E., Spall, M. A., & Thompson, A. F. (2016). A theory of the wind-driven Beaufort Gyre variability. *Journal of Physical Oceanography*, *46*, 3263–3278. https://doi.org/10.1175/JPO-D-16-0091.1

Martin, T., Tsamados, M., Schroeder, D., & Feltham, D. L. (2016). The impact of variable sea ice roughness on changes in Arctic Ocean surface stress: A model study. *Journal of Geophysical Research: Oceans*, *121*, 1931–1952. https://doi.org/10.1002/2015JC011186

Mayer-Gürr, T., Rieser, D., Höck, E., Brockmann, J. M., Schuh, W.-D., Krasbutter, I., et al. (2012). The new combined satellite only model GOCO03s, poster presented at GGHS2012 Meeting, Gravity Observation and Combination project, Initiated by the ESA GOCE AO (project no 4248). Venice, Italy.

McLaughlin, F. A., Carmack, E. C., Macdonald, R. W., Melling, H., Swift, J. H., Wheeler, P. A., et al. (2004). The joint roles of Pacific and Atlantic-origin waters in the Canada Basin, 1997–1998. *Deep Sea Research Part I*, *51*, 107–128.

McLaughlin, F. A., Carmack, E. C., Williams, W. J., Zimmermann, S., Shimada, K., & Itoh, M. (2009). Joint effects of boundary currents and thermohaline intrusions on the warming of Atlantic Water in the Canada Basin, 1993–2007. *Journal of Geophysical Research*, *114*, C00A12. https://doi.org/10.1029/2008JC005001

McPhee, M. G. (1980). An analysis of pack ice drift in summer. In R. Pritchard (Ed.), *Sea ice processes and models* (pp. 62–75). Seattle: University of Washington Press.

McPhee, M. G. (2013). Intensification of geostrophic currents in the Canada Basin, Arctic Ocean. *Journal of Climate*, *26*, 3130–3138. https://doi.org/10.1175/JCLI-D-12-00289.1

Meneghello, G., Marshall, J., Campin, J.-M., Doddridge, E., & Timmermans, M.-L. (2018). The Ice-Ocean Governor: Ice-ocean stress feedback limits Beaufort Gyre spin up. *Geophysical Research Letters*, *45*, 11,293–11,299. https://doi.org/10.1029/2018GL080171

Meneghello, G., Marshall, J., Cole, S.-T., & Timmermans, M.-L. (2017). Observational inferences of lateral eddy diffusivity in the halocline of the Beaufort Gyre. *Geophysical Research Letters*, *44*, 12,331–12,338. https://doi.org/10.1002/2017GL075126

Meneghello, G., Marshall, J., Timmermans, M.-L., & Scott, J. (2018). Observations of seasonal upwelling and downwelling in the Beaufort Sea mediated by sea ice. *Journal of Physical Oceanography*, *48*(4), 795–805. https://doi.org/10.1175/JPO-D-17-0188.1

Moore, G. W. K. (2012). Decadal variability and a recent amplification of the summer Beaufort Sea High. *Geophysical Research Letters*, *39*, L10807. https://doi.org/10.1029/2012GL051570

Morison, J., Kwok, R., Peralta-Ferriz, C., Alkire, M., Rigor, I., Andersen, R., & Steele, M. (2012). Changing Arctic Ocean freshwater pathways. *Nature*, *481*, 66–70. https://doi.org/10.1038/nature10705

Peralta-Ferriz, C., & Morison, J. (2010). Understanding the annual cycle of the Arctic Ocean bottom pressure. *Geophysical Research Letters*, *37*, L10603. https://doi.org/10.1029/2010GL042827

Peralta-Ferriz, C., & Woodgate, R. A. (2017). The dominant role of the East Siberian Sea in driving the oceanic flow through Bering Strait—Conclusions from GRACE ocean mass satellite data and in situ mooring observations between 2002 and 2016. *Geophysical Research Letters*, *44*, 11,472–11,481. https://doi.org/10.1002/2017GL075179

Petty, A. A., Hutchings, J. K., Richter-Menge, J. A., & Tschudi, M. A. (2016). Sea ice circulation around the Beaufort Gyre: The changing role of wind forcing and the sea ice state. *Journal of Geophysical Research: Oceans*, *121*, 3278–3296. https://doi.org/10.1002/2015JC010903

Pickart, R. S., Spall, M. A., & Mathis, J. T. (2013). Dynamics of upwelling in the Alaskan Beaufort Sea and associated shelf-basin fluxes. *Deep-Sea Research Part I*, *76*, 35–51.

Proshutinsky, A. Y., Bourke, R. H., & McLaughlin, F. A. (2002). The role of the Beaufort Gyre in Arctic climate variability: Seasonal to decadal climate scales. *Geophysical Research Letters*, *29*(23), 2100. https://doi.org/10.1029/2002GL015847

Proshutinsky, A., Dukhovskoy, D., Timmermans, M.-L., Krishfield, R., & Bamber, J. L. (2015). Arctic circulation regimes. *Philosophical Transactions A*, *373*, 20140160. https://doi.org/10.1098/rsta.2014.0160

Proshutinsky, A. Y., & Johnson, M. A. (1997). Two circulation regimes of the wind-driven Arctic Ocean. *Journal of Geophysical Research*, *102*, 12,493–12,514. https://doi.org/10.1029/97JC00738

Proshutinsky, A., Krishfield, R., Timmermans, M.-L., Toole, J., Carmack, E., McLaughlin, F., et al. (2009). Beaufort Gyre freshwater reservoir: State and variability from observations. *Journal of Geophysical Research*, *114*(C00A10). https://doi.org/10.1029/2008JC005104

Rabe, B., Karcher, M., Kauker, F., Schauer, U., Toole, J. M., Krishfield, R. A., et al. (2014). Arctic Ocean basin liquid freshwater storage trend 1992–2012. *Geophysical Research Letters*, *41*, 961–968. https://doi.org/10.1002/2013GL058121

Rabe, B., Karcher, M., Schauer, U., Toole, J. M., Krishfield, R. A., Pisarev, S., et al. (2011). An assessment of Arctic Ocean freshwater content changes from the 1990s to the 2006–2008 period. *Deep Sea Research Part I*, *58*(2), 173–185.

Serreze, M. C., & Barrett, A. P. (2011). Characteristics of the Beaufort Sea High. *Journal of Climate*, *24*, 159–182.

Serreze, M. C., Barrett, A. P., Slater, A. G., Woodgate, R. A., Aagaard, K., Lammers, R. B., et al. (2006). The large-scale freshwater cycle of the Arctic. *Journal of Geophysical Research*, *111*, C11010. https://doi.org/10.1029/2005JC003424

Simmonds, I., & Rudeva, I. (2012). The great Arctic cyclone of August 2012. *Geophysical Research Letters*, *39*, L23709. https://doi.org/10.1029/2012GL054259

Timmermans, M.-L., Marshall, J., Proshutinsky, A., & Scott, J. (2017). Seasonally-derived components of the Canada Basin halocline. *Geophysical Research Letters*, *44*, 5008–5015. https://doi.org/10.1002/2017GL073042

Timmermans, M.-L., Proshutinsky, A., Golubeva, E., Jackson, J. M., Krishfield, R., McCall, M., et al. (2014). Mechanisms of Pacific summer water variability in the Arctic's central Canada basin. *Journal of Geophysical Research: Oceans*, *119*, 7523–7548. https://doi.org/10.1002/2014JC010273

Tschudi, M., Fowler, C., Maslanik, J., Stewart, J. S., & Meier, W. (2016). Polar Pathfinder daily 25 km EASE-grid sea ice motion vectors, 3 (Northern Hemisphere). Boulder, CO: National Snow and Ice Data Center. https://doi.org/10.5067/O57VAIT2AYYY

Weatherall, P., Marks, K. M., Jakobsson, M., Schmitt, T., Tani, S., Arndt, J. E., et al. (2015). A new digital bathymetric model of the world's oceans, vol. *2*, pp. 331–345. https://doi.org/10.1002/2015EA000107

Woodgate, R. A. (2018). Increases in the Pacific inflow to the Arctic from 1990–2015, and insights into seasonal trends and driving mechanisms from year-round Bering Strait mooring data. *Progress in Oceanography*, *160*, 124–154.

Woodgate, R. A., Aagaard, K., Swift, J. H., W. M. Smethie Jr, & Falkner, K. K. (2007). Atlantic Water circulation over the Mendeleev Ridge and Chukchi Borderland from thermohaline intrusions and water mass properties. *Journal of Geophysical Research*, *112*, C02005. https://doi.org/10.1029/2005JC003416

Yang, J., Proshutinsky, A., & Lin, X. (2016). Dynamics of an idealized Beaufort Gyre: 1. The effect of a small beta and lack of western boundaries. *Journal of Geophysical Research: Oceans*, *121*, 1249–1261. https://doi.org/10.1002/2015JC011296

Zhang, J., Lindsay, R., Steele, M., & Schweiger, A. (2008). What drove the dramatic retreat of Arctic sea ice during summer 2007? *Geophysical Research Letters*, *35*, L11505. https://doi.org/10.1029/2008GL034005

Zhang, J., Steele, M., Runciman, K., Dewey, S., Morison, J., Lee, C., et al. (2016). The Beaufort Gyre intensification and stabilization: A model-observation synthesis. *Journal of Geophysical Research: Oceans*, *121*, 7933–7952. https://doi.org/10.1002/2016JC012196

Zhao, M., & Timmermans, M. (2018). Topographic Rossby waves in the Arctic Ocean's Beaufort Gyre. *Journal of Geophysical Research: Oceans*, *123*, 6521–6530. https://doi.org/10.1029/2018JC014233

Zhao, M., Timmermans, M., Cole, S., Krishfield, R., & Toole, J. (2016). Evolution of the eddy field in the Arctic Ocean's Canada Basin, 2005–2015. *Geophysical Research Letters*, *43*, 8106–8114. https://doi.org/10.1002/2016GL069671

Zhong, W., Steele, M., Zhang, J., & Zhao, J. (2018). Greater role of geostrophic currents in Ekman dynamics in the western Arctic Ocean as a mechanism for Beaufort Gyre stabilization. *Journal of Geophysical Research: Oceans*, *123*, 149–165. https://doi.org/10.1002/2017JC013282

Zhong, W., & Zhao, J. (2014). Deepening of the Atlantic Water core in the Canada Basin in 2003–11. *Journal of Physical Oceanography*, *44*, 2353–2369.